

基于主动散斑投射的水下双目视觉 三维成像

庄苏锋, 屠大维*, 刘建业

上海大学机电工程与自动化学院, 上海 200072

摘要 基于主动散斑投射的双目立体视觉成像技术仅需一次投影拍摄即可实现三维重建, 适合于动态成像, 但在水下应用时, 存在小孔模型失效、极线约束匹配条件不满足, 以及投射散斑左右图像因受水下环境吸收、散射影响产生退化等问题。本文重新建立了基于主动投射散斑图案的水下双目视觉成像模型, 分析了散斑图案对水下双目对应点匹配精度的影响, 搭建了主动散斑水下双目视觉动态三维成像系统实验装置。实验结果表明, 基于主动散斑投射的水下双目立体视觉技术具有较好的动态 3D 成像效果, 动态误差在该双目立体视觉实验装置本身结构和系统参数决定的静态误差之内。

关键词 成像系统; 水下双目立体视觉; 动态三维成像; 水下三维重建; 主动散斑投射

中图分类号 TP39; TH74 **文献标志码** A

DOI: 10.3788/AOS230503

1 引言

在视觉引导机器人作业应用场景, 当目标与视觉系统之间存在相对运动时, 需要动态获取场景中目标的三维图像。双目立体视觉可以同步快速获得左右相机的图像, 相比于激光雷达、线扫描结构光等以扫描为特征的三维成像方式, 具有更好的动态适应性^[1-5]。双目立体视觉辅以主动散斑投射照明, 可增强目标表面的纹理信息, 提高左、右图像对应点的匹配精度, 是一种常用的手段。目前对空气中应用的主动散斑投射双目立体视觉系统的研究较为成熟^[6-10], 并已有商业化产品, 如微软的 Kinect 系统、Correlation Solutions 公司的 Vic-3D 测量系统、德国 Dantec 公司的 Q-400 系统等; 水下应用时, 双目立体视觉系统存在小孔模型失效、极线约束匹配条件不满足, 以及投射散斑左右图像由于受到水下环境吸收、散射的影响而产生退化等问题^[11-14]。

本文重新建立了基于主动投射散斑图案的水下双目视觉成像模型, 分析了散斑图案对水下双目对应点匹配精度的影响, 建立了主动散斑水下双目视觉动态三维成像系统实验装置。实验结果表明, 基于主动散斑投射的水下双目立体视觉技术具有较好的动态 3D 成像效果, 动态误差在由该双目立体视觉实验装置本身结构和系统参数决定的静态误差之内。

2 主动投射散斑的水下立体视觉成像原理

2.1 系统组成

主动投射散斑的水下双目立体视觉成像装置主要由一个散斑图案投射器和两台相机组成, 散斑图案投射器可采用空间光调制器或投影仪。本实验使用的散斑图案投射器是投影仪, 由计算机生成的散斑图案经投影仪投射到水下目标, 左、右相机同步快速拍摄表面附有散斑图案的水下运动物体, 按照双目立体视觉原理, 计算得到水下目标的三维图像。系统组成如图 1 所示。

2.2 散斑的产生

计算机按照一定的数学规律产生散斑图案, 并需要根据需要改变散斑大小和密度等参数。本文将计算机产生的可在屏幕上显示的所有散斑称为散斑图案, 定义散斑大小为单个散斑占据的像素数量, 定义散斑密度为散斑总数量与图像总像素的比值。显然, 散斑大小与散斑密度是相互制约的。图 2 所示为得到的两幅散斑图案: 图 2(a) 所示图案的散斑密度为 1%, 散斑大小为 4 pixel, 每个散斑的尺寸为 2 pixel × 2 pixel, 如图 2(a) 右上角所示; 图 2(b) 所示图案的散斑密度为 2%, 散斑大小为 9 pixel, 每个散斑的尺寸为 3 pixel × 3 pixel, 如图 2(b) 右上角所示。

投影机投射的散斑被水下相机拍摄, 所得到的散

收稿日期: 2023-02-03; 修回日期: 2023-03-01; 录用日期: 2023-04-06; 网络首发日期: 2023-05-16

基金项目: 国家自然科学基金(62176149, 61673252)

通信作者: *tdw@shu.edu.cn

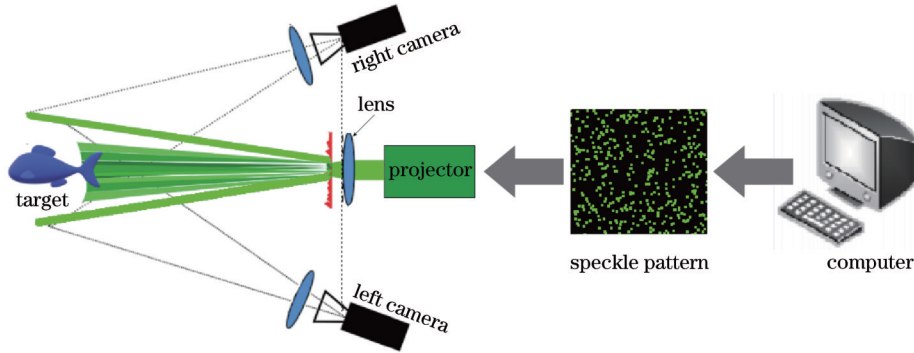


图 1 基于主动投射散斑的水下双目视觉成像系统

Fig. 1 Underwater binocular vision imaging system based on active speckle projection

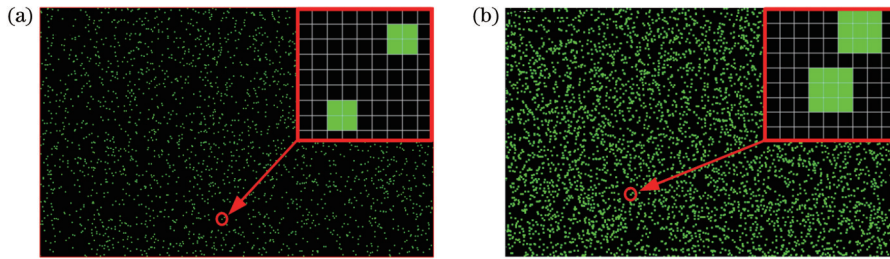


图 2 计算机产生的散斑图案。(a)散斑密度为 1%，散斑大小为 4 pixel，散斑尺寸为 2 pixel×2 pixel；(b)散斑密度为 2%，散斑大小为 9 pixel，散斑尺寸为 3 pixel×3 pixel

Fig. 2 Speckle patterns generated by the computer. (a) Speckle density is 1%, speckle size is 4 pixel, and size of each speckle is 2 pixel×2 pixel; (b) speckle density is 2%, speckle size is 9 pixel, and size of each speckle is 3 pixel×3 pixel

斑图像称为图像散斑。目前,计算机屏幕显示的散斑图案的大小、密度,投影仪投射散斑的大小、密度,以及水下相机拍摄到的图像散斑的大小、密度没有统一定义,且通常情况下三者是不一致的。为简单起见,本文假设计算机屏幕显示的散斑图案与投影机在水下投射的散斑相同,在投影机选定,即画面投射比(投影距离

与画面宽度之比)指标确定后,通过选择水下相机的光敏面尺寸及焦距,使焦距与光敏面尺寸比等于投影仪画面投射比(图 3),这样水下相机拍摄的图像散斑大小、密度与投影仪在水下投射的散斑大小、密度一致。计算机生成的散斑图案的性质决定了主动水下投射的散斑及水下相机接收的图像散斑的性质。

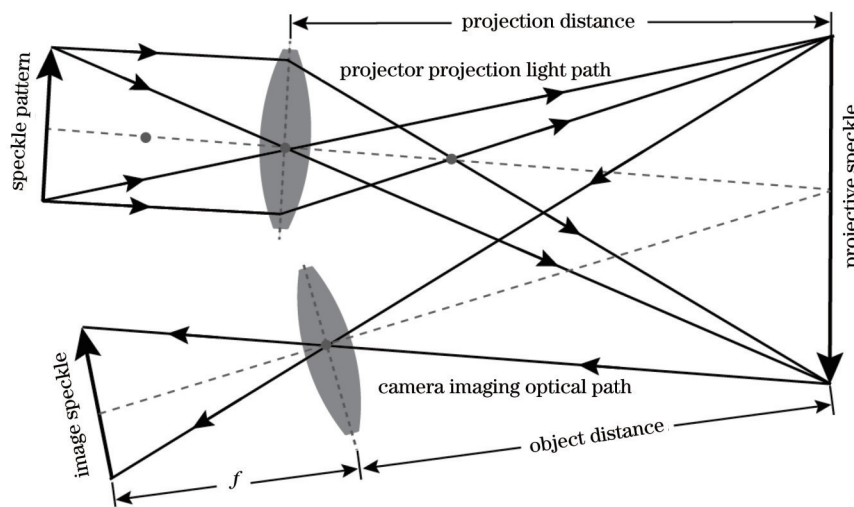


图 3 水下主动散斑投射与相机成像

Fig. 3 Underwater active speckle projection and camera imaging

2.3 水下双目视觉成像模型及对应点匹配计算

在水下双目立体相机视觉测量系统中,相机被封

装在具有玻璃窗口的防水舱内,成像光线从水中进入空气经过折射后成像,传统的摄像机模型失效,左右图

像对应点匹配的极线约束条件没有得到满足^[15], 因此需要建立新的成像模型。

假设投影仪坐标系与世界坐标系重合, 投射散斑图案上某一像素点 $p_1(u_1, v_1)$, 经过投影仪投射至目标表面后的对应点为 $P(X_w, Y_w, Z_w)$, 经左相机采集的图像散斑上的对应点为 $p_l(u_l, v_l)$, 经右相机采集的图像散斑上的对应点为 $p_r(u_r, v_r)$, 如图 4 所示。相机坐标系相对于投影仪坐标系的关系为 $[R, T]$, 右相机坐标

系相对于左相机坐标系的关系为 $[R_1, T_1]$ 。

所建立的主动投射散斑的水下双目立体视觉成像模型如图 5 所示。将投影仪坐标系原点 (X_p, Y_p, Z_p) 建立在投影仪镜头光心 O_p 上, 并将 X_p 轴的方向定义为投影仪镜头光心 O_p 与右相机镜头光心 O_r 的连线方向。折射坐标系原点 (X_r, Y_r, Z_r) 与投影仪镜头光心 O_p 重合, 并将 Z_r 轴的正方向定义为水与空气的分界面法线方向。

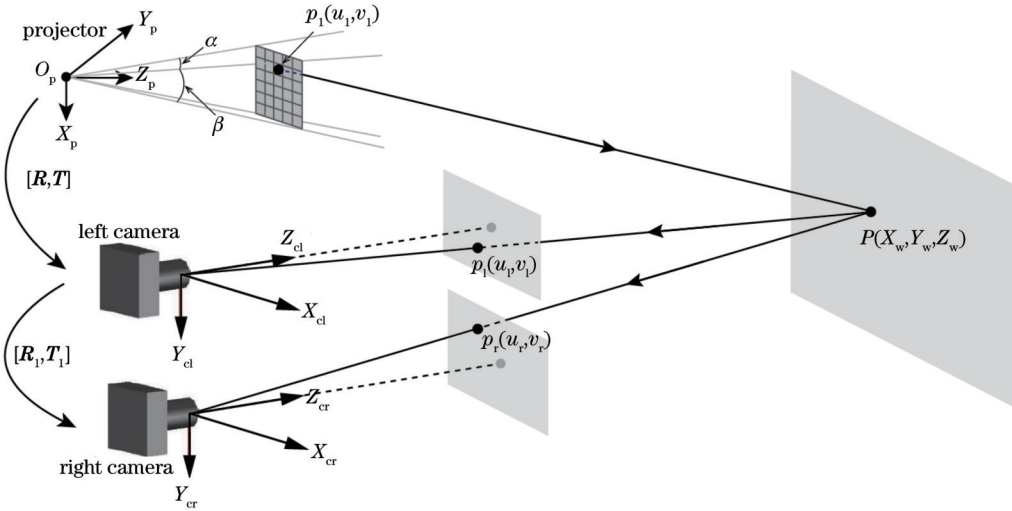


图 4 主动投射散斑双目立体成像示意图

Fig. 4 Schematic of active projection speckle binocular stereo imaging

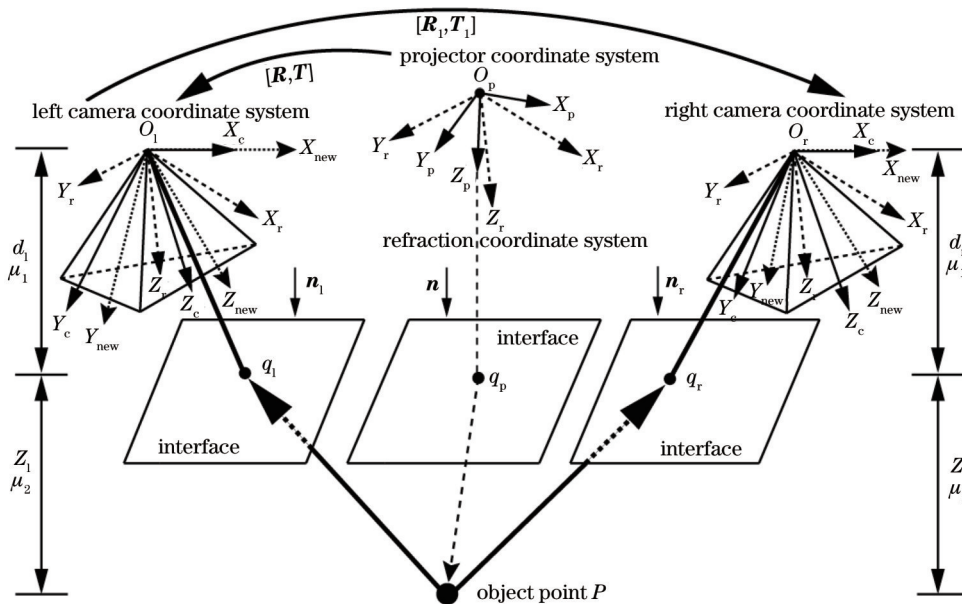


图 5 主动投射散斑的水下双目立体视觉成像模型

Fig. 5 Underwater binocular stereo camera imaging model with active speckle projection

折射坐标系与投影仪坐标系之间的关系为

$$\begin{cases} P_p = R_r^{(p)} P_r + t_r^{(p)} \\ R_r^{(p)} = \begin{bmatrix} n \times z_p & n \times (n \times z_p) & n \end{bmatrix}, \\ t_r^{(p)} = [0 \ 0 \ 0]^T \\ z_p = [0 \ 0 \ 1]^T \end{cases}, \quad (1)$$

式中: P_p 为投影仪坐标系下的三维点坐标; P_r 为折射坐标系下的三维坐标; n 为投影仪坐标系下分界面的法向量。

投影仪坐标系下物点 P 与像点 $p_1 = [u_1 \ v_1]^T$ 的关系为

$$\tilde{p}_1 = KP, \quad (2)$$

式中: K 为投影仪成像系统内参矩阵。

任意像点 p_1 决定一条光线, 在投影仪坐标系下, 光线方向表示为

$$I_p = \frac{K^{-1} \tilde{p}_1}{\|K^{-1} \tilde{p}_1\|} \quad (3)$$

将光线转换到折射坐标系下, 有

$$I_r = R_p^{(r)} I_p = [R_p^{(p)}]^{-1} I_p \quad (4)$$

利用光线四维参数表示法^[16]描述光线, 得到

$$L_r = \begin{bmatrix} \frac{1}{I_r(3)} & 0 \\ 0 & \frac{1}{I_r(3)} \\ 0 & 0 \end{bmatrix}^T, \quad (5)$$

式中: $I_r(3)$ 为光线方向矩阵 I_r 的第 3 列。

光线传播一定距离 d_1 后发生折射, 折射后的光线表示为

$$L' = R(s, t, \mu_1, \mu_2) \otimes T(d_1) \otimes L_r = \begin{bmatrix} 1 & & & \\ & 1 & & \\ & & \alpha & \\ & & & \beta \end{bmatrix} \otimes \begin{bmatrix} 1 & d_1 \\ & 1 \\ & & 1 \\ & & & 1 \end{bmatrix} \otimes L_r, \quad (6)$$

式中: μ_1 和 μ_2 分别为入射介质(空气)的折射率和出射介质(水)的折射率; $\alpha = [s \ t \ \mu_1 \ \mu_2]^T$ 和 $\beta = [s \ t \ \mu_1 \ \mu_2]^T$ 为经过折射后光线方向变化的待定参数^[17]。

折射后的光线在传播距离 Z_1 后表示为

$$L'' = T(Z_1) \otimes L' = \begin{bmatrix} 1 & & Z_1 & \\ & 1 & & Z_1 \\ & & 1 & \\ & & & 1 \end{bmatrix} \otimes \begin{bmatrix} 1 & & & \\ & 1 & & \\ & & \alpha & \\ & & & \beta \end{bmatrix} \otimes \begin{bmatrix} 1 & d_1 \\ & 1 \\ & & 1 \\ & & & 1 \end{bmatrix} \otimes L_r \quad (7)$$

水下物点 P 的坐标值的确定过程^[17]如下: 以左相机成像为例, 光线 L'' 传播距离 Z_1 后到达水和空气的分界面 q_1 处, 并发生折射, 折射后的光线表达为

$$L_1'' = R(s, t, \mu_1, \mu_2) \otimes T(Z_1) \otimes L''; \quad (8)$$

以上光线继续传播距离 d_1 后到达成像平面, 光线表达为

$$L_1''' = T(Z_1) \otimes L_1'' \quad (9)$$

将上述光线 L_1''' 转换到左平面折射坐标系下, 得到的光线 L_{c-1} 包含了成像点的方向数据 $a^{(l)}$ 和位置信息 $q^{(l)}$ 。同理, 可得其在右平面折射坐标系下的对应光线 L_{c-r} , 该光线亦包含了对应匹配像点的方向数据 $a^{(r)}$ 和位置信息 $q^{(r)}$ 。鉴于物点 P (图 5 中的点 P) 同时处于左、右平面折射坐标系上, 因此满足以下约束^[18]:

$$\begin{cases} a^{(l)} \times [P - q^{(l)}] = 0 \\ a^{(r)} \times [P - q^{(r)}] = 0 \end{cases} \quad (10)$$

使用反对称矩阵表示向量积, 式(10)可转化为

$$\begin{cases} [a^{(l)}]_x \cdot [P - q^{(l)}] = 0 \\ [a^{(r)}]_x \cdot [P - q^{(r)}] = 0 \end{cases}, \quad (11)$$

式中: $[\cdot]_x$ 为向量积的反对称矩阵表达形式。

对式(11)进行奇异值分解, 可得到 P 的三维坐标。同理, 对所有匹配像点执行上述操作, 即可得到水下目标的三维点云。

2.4 仿真与分析

利用 MATLAB 2015b 软件仿真分析散斑图案与

水下双目成像匹配精度的关系。设置相机的物距为 2800 mm, 空气折射率为 1, 水的折射率为 1.333。当散斑密度为 2% 时, 研究散斑大小对匹配精度的影响, 仿真结果如图 6 所示。可看出: 随着散斑增大, 最大匹配误差先降低后升高; 当散斑大小为 3~15 pixel 时, 最大匹配误差都小于 0.7 pixel; 当散斑大小为 9 pixel 时, 匹配精度最高。这是因为在散斑密度一定的情况下, 散斑太大或太小都不利于匹配, 大小合适的散斑能增强左右相机图像对应点匹配线索。

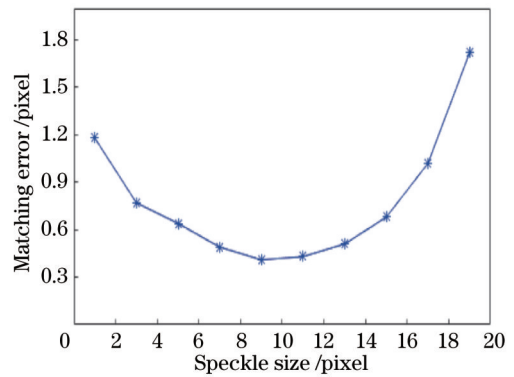


图 6 散斑大小对匹配精度的影响

Fig. 6 Influence of the speckle size on matching accuracy

图 7 所示为散斑大小为 9 pixel 时, 散斑密度对匹配精度的影响。可看出: 随着散斑密度的增加, 最大匹配误差先下降后上升; 当散斑密度为 1.5%~3.5% 时, 匹配误差都小于 0.6 pixel; 当散斑密度为 2% 时,

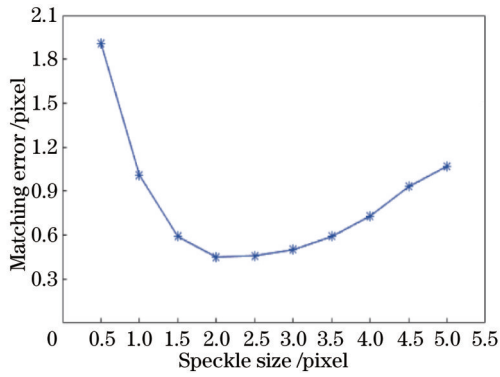
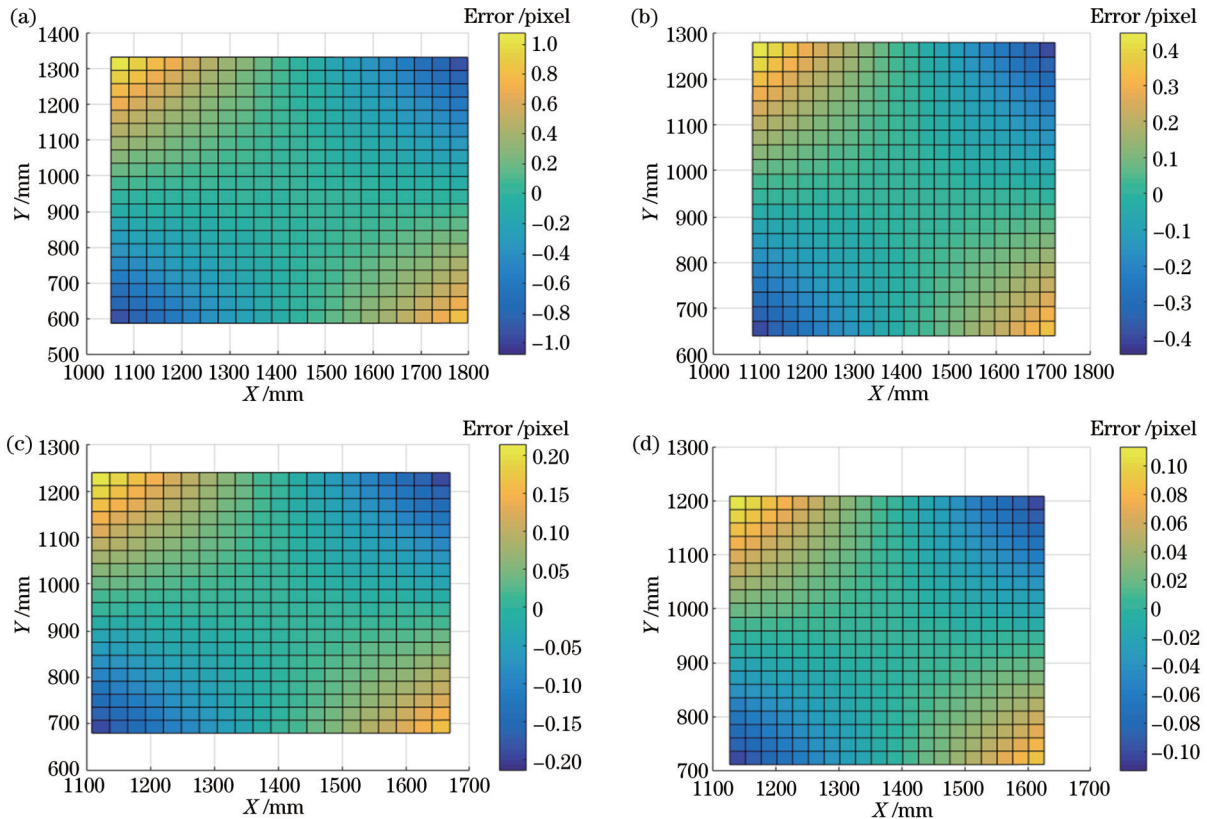


图 7 散斑密度对匹配精度的影响

Fig. 7 Influence of speckle density on matching accuracy

图 8 不同距离对应点匹配误差。(a) $Z=2400$ mm; (b) $Z=2800$ mm; (c) $Z=3200$ mm; (d) $Z=3600$ mmFig. 8 Matching error of corresponding points at different distances. (a) $Z=2400$ mm; (b) $Z=2800$ mm; (c) $Z=3200$ mm; (d) $Z=3600$ mm

3 实验装置

实验装置主要由投影仪和水下双目立体视觉装置组成(图 9)。投影仪采用 EPSON 950WH:亮度为 3000 lm,对比度为 10000:1,画面投射比约为 1.27。水下双目立体视觉系统的分辨率、作用距离、成像范围、景深主要由基线距离、镜头焦距和相机光敏面尺寸和像元大小等系统结构和参数决定。选用大恒相机 MER2-1220-32U3M/C,光敏面尺寸为 1/1.7 inch (1 inch=2.54 cm),像元尺寸为 $1.85 \mu\text{m} \times 1.85 \mu\text{m}$,分辨率为 $4024 \text{ pixel} \times 3036 \text{ pixel}$;选用 Kowa 镜头

匹配精度最高。这是因为在散斑大小一定的情况下,散斑太密集,以至于混在一起难以区分,显然不利于特征匹配,但散斑太稀疏,也难以从相邻散斑中搜寻到匹配特征,因此合适的散斑密度有利于提高散斑匹配精度。

图 8 所示为散斑大小为 9 pixel 和散斑密度为 2% 时,水下双目相机物距分别在 2400 mm、2800 mm、3200 mm 和 3600 mm 时的匹配误差,其中横、纵轴表示视场范围。从仿真结果可看出,基于上述仿真参数,在 2.4~3.6 m 范围内,随着物距减小,最大匹配误差逐渐增加,但仍小于 1.1 pixel,具有较高的匹配精度。

LM12JC10M,焦距为 12 mm(光敏面尺寸与焦距之比为 0.784);左相机镜头光心与右相机镜头光心的距离为 350 mm。此时,水下双目立体成像系统在像素匹配误差为 1 pixel 的前提下,理论上在 2~3.2 m 成像距离范围内的静态测量误差(标准差)为 3.5 mm,该误差是由系统结构和参数决定的,是系统的固有静态误差。

对于图 9 所示的由两台相机固定组成的水下双目立体成像系统,需要对系统内外参数进行标定。先利用迭代标定法获取空气中的相机参数,再进行水下标定^[18]。上述实验装置的系统标定参数如表 1 所示。其

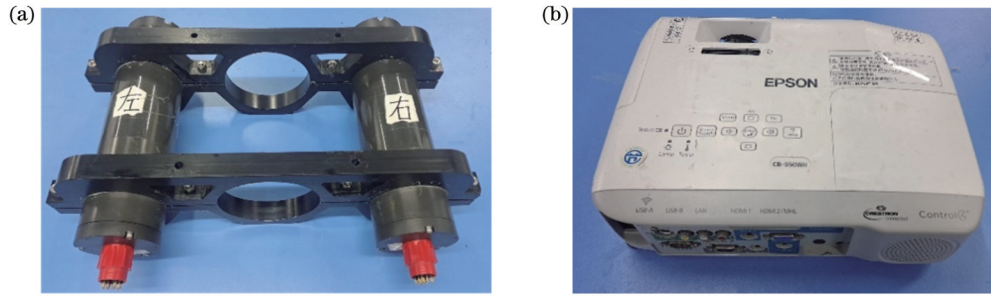


图 9 实验装置。(a)水下双目立体视觉装置;(b)投影仪

Fig. 9 Experimental equipment. (a) Underwater binocular stereo vision device; (b) projector

中, (f_x, f_y) 为相机等效焦距, (u_0, v_0) 为主点坐标, $k_c(k_1, k_2, k_3, p_1, p_2)$ 为畸变系数, E_1 为空气中左、右相机标定的重投影误差, n 为折射平面法向量, d 为光心到折射面的距离, R_a 为空气中左、右相机坐标系之间的旋

转矩阵, T_a 为空气中左、右相机坐标系之间的平移矩阵, R_w 为水中左、右折射坐标系之间的旋转矩阵, T_w 为水中左、右折射坐标系之间的平移矩阵, E_2 为水下双目立体标定的重投影误差。

表 1 主动散斑水下双目立体成像系统标定参数

Table 1 Calibration parameters of active speckle underwater binocular vision imaging system

Parameter	Left camera	Right camera
(f_x, f_y)	(6763.1897, 6763.8273)	(6761.4365, 6761.4764)
(u_0, v_0)	(2041.5508, 1451.1157)	(2135.5726, 1498.5434)
$k_c(k_1, k_2, k_3, p_1, p_2)$	(-0.01825, 0.06559, 0.00134)	(-0.02241, 0.13610, 0.00037)
E_1	0.0224	0.0235
n	[0.002398 0.013658]	[-0.002076 0.010830]
d/mm	71.9455	74.9998
R_a/mm	[-0.0028 -0.0024 0.0380]	
T_a/mm	[-352.0986 -7.6429 8.4047]	
R_w/mm	[-0.0056 0.0016 0.0380]	
T_w/mm	[-352.0805 -7.7374 9.0523]	
E_2	0.2304	

4 水下动态三维成像精度实验

本实验的目的是考察所建立的双目立体视觉三维成像实验装置水下三维成像的动态误差情况。搭建的实验场景如图 10 所示, 并将投影仪与计算机相连; 基于以上仿真结果, 计算机产生的散斑密度为 2%, 散斑大小为 9 pixel, 投影仪将散斑图案斜向下投射到水下

被测目标表面。水下被测目标为一个标准球(其直径由上海市计量测试技术研究院预先标定, 标定值为 199.802 mm)。标准球由细绳悬挂于实验装置前方约 3 m 远处。

如图 11 所示, 标准球在与两台相机平行的平面上摆动(起始角度约为 50° , 0 初速释放后自由摆动), 在不同位置具有不同的瞬时线速度, 到达最低点时具

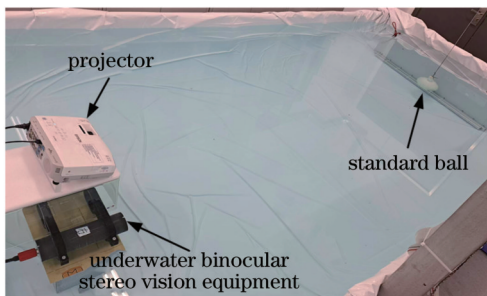


图 10 实验场景

Fig. 10 Experiment scene

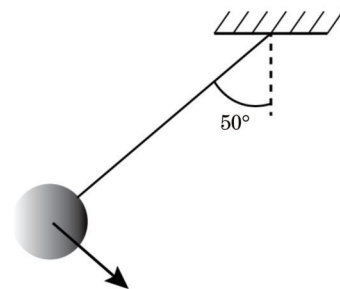


图 11 水下目标运动示意图

Fig. 11 Motion diagram of underwater target

有最大瞬时速度,测得该最大瞬时速度为 1.2 m/s。图 12 所示为左相机采集的标准球在水下摆动时 4 个位置的图像,其中第 3 帧为最低处的照片。

基于采集的左、右图像,即可计算出三维点云数据,

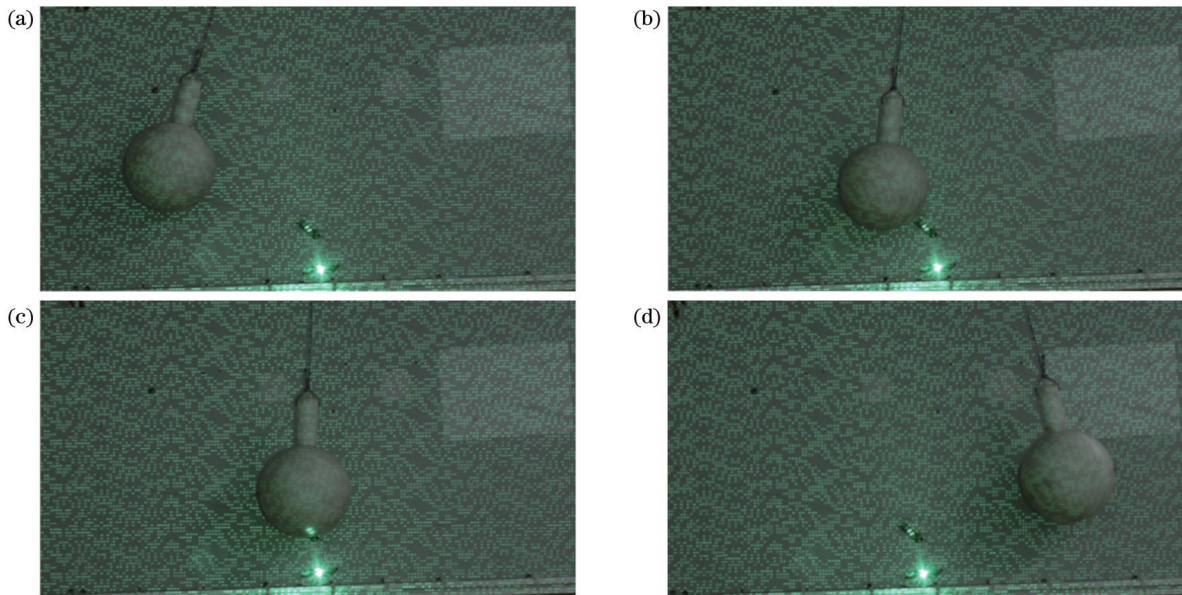


图 12 左相机采集的水下图像。(a)第 1 帧图像;(b)第 2 帧图像;(c)第 3 帧图像;(d)第 4 帧图像

Fig. 12 Underwater images acquired by left camera. (a) Image of frame 1; (b) image of frame 2; (c) image of frame 3; (d) image of frame 4

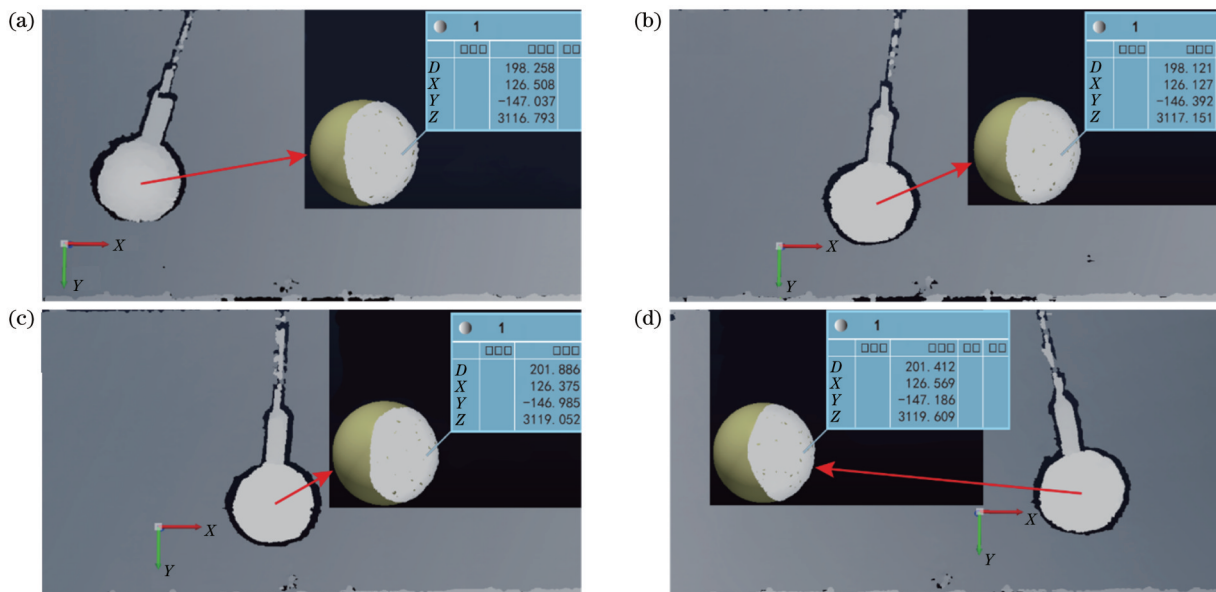


图 13 不同运动位置的三维点云及拟合球体。(a)第 1 帧三维点云;(b)第 2 帧三维点云;(c)第 3 帧三维点云;(d)第 4 帧三维点云

Fig. 13 3D point cloud and fitting sphere at different motion positions. (a) 3D point cloud at frame 1; (b) 3D point cloud at frame 2; (c) 3D point cloud at frame 3; (d) 3D point cloud at frame 4

多次重复上述动态成像实验,标准球在最低点处的直径误差及其多次测量结果的标准差(SD)如表 2 所示。实验结果表明:标准球在最大瞬时速度时动态误差的标准差为 2.4 mm,该标准差值在实验装置本身结构和系统参数决定的最大固有静态精度(3.5 mm)之内。

图 13 所示为图 12 对应位置的三维点云图像。使用 PolyWorks 软件将得到的三维点云拟合为球体(图 13 插图),得到球的直径与球心坐标(图 13 插图右上角数据),并与标准球直径 D 进行比较,即得到动态测量误差。

5 结 论

对基于主动散斑投射的水下双目立体视觉动态成像技术进行研究,分析了主动投射散斑图案对水下双目立体视觉对应点匹配精度的影响,搭建了主动散斑水下双目视觉动态三维成像系统实验装置。实验结果

表 2 标准球测量误差及其标准差
Table 2 Error and standard deviation of standard ball

No.	Measurement value of ball diameter at the maximum instantaneous speed (the lowest point) /mm	Error /mm	SD /mm
1	201.9	2.1	
2	202.5	2.7	
3	202.3	2.5	
4	202.1	2.3	
5	202.2	2.4	
6	202.4	2.6	2.4
7	202.1	2.3	
8	201.7	1.9	
9	202.4	2.6	
10	202.6	2.8	

表明,基于主动散斑投射的水下双目立体视觉技术具有较好的动态 3D 成像效果,动态误差在该双目立体视觉实验装置本身结构和系统参数决定的静态误差之内。需要说明的是:本文主要研究水下主动散斑投射双目立体视觉系统对水下运动目标的适应性,关于水体扰动及折射率变化影响将另文单独阐述。

参 考 文 献

- [1] 江荣,朱攀,周兴林,等.基于双目视觉算法的路面三维纹理信息获取[J].激光与光电子学进展,2022,59(14):1415026.
Jiang R, Zhu P, Zhou X L, et al. Obtaining 3D texture information of pavement based on binocular vision algorithm[J]. Laser & Optoelectronics Progress, 2022, 59(14): 1415026.
- [2] Yue H S, Yu Y, Chen W H, et al. Accurate three dimensional body scanning system based on structured light[J]. Optics Express, 2018, 26(22): 28544-28559.
- [3] 冉舒文,刘显明,雷小华,等.基于双目视觉的抬头显示虚像三维形貌测量[J].光学学报,2022,42(19):1912001.
Ran S W, Liu X M, Lei X H, et al. Three-dimensional shape measurement of virtual image of head-up display based on binocular vision[J]. Acta Optica Sinica, 2022, 42(19): 1912001.
- [4] 胡亮,段慧仙,裴浩东,等.非合作航天器关键特征的双目视觉位姿测量[J].中国激光,2022,49(17):1704003.
Hu L, Duan H X, Pei H D, et al. Binocular vision pose measurement of key features of non-cooperative spacecraft[J]. Chinese Journal of Lasers, 2022, 49(17): 1704003.
- [5] 周骛,王芳婷,王宵宵,等.基于双目视觉多曝光的粒子轨迹测速方法研究[J].光学学报,2021,41(12):1215001.
Zhou W, Wang F T, Wang X X, et al. Particle streak velocimetry method based on binocular vision and multiple exposure[J]. Acta Optica Sinica, 2021, 41(12): 1215001.
- [6] Schaffer M, Grosse M, Kowarschik R. High-speed pattern projection for three-dimensional shape measurement using laser speckles[J]. Applied Optics, 2010, 49(18): 3622-3629.
- [7] Yin X W, Wang G J, Shi C B, et al. Efficient active depth sensing by laser speckle projection system[J]. Optical Engineering, 2014, 53(1): 013105.
- [8] Heist S, Lutzke P, Dietrich P, et al. Experimental comparison of laser speckle projection and array projection for high-speed 3D measurements[J]. Proceedings of SPIE, 2015, 9525: 952515.
- [9] 潘创,刘乙奇,黄道平.基于激光散斑的实时立体匹配算法及其应用[J].华南理工大学学报(自然科学版),2020,48(8):22-28.
Pan C, Liu Y Q, Huang D P. Laser speckle-based real-time stereo matching algorithm and its application[J]. Journal of South China University of Technology (Natural Science Edition), 2020, 48(8): 22-28.
- [10] 李晓侠,孙长库,孙玉晶,等.结合描述子信息的多约束散斑扩散匹配方法[J].激光与光电子学进展,2023,60(6):0611003.
Li X X, Sun C K, Sun Y J, et al. Multi-constrained speckle propagation matching method combined with descriptor information[J]. Laser & Optoelectronics Progress, 2023, 60(6): 0611003.
- [11] 解则晓,余江姝,迟书凯,等.非平行双目视觉系统水下标定与测量[J].光学学报,2019,39(9):0912004.
Xie Z X, Yu J S, Chi S K, et al. Underwater calibration and measurement based on non-parallel stereovision[J]. Acta Optica Sinica, 2019, 39(9): 0912004.
- [12] Wu H D, Zhao M, Xu W H. Underwater de-scattering imaging by laser field synchronous scanning[J]. Optics and Lasers in Engineering, 2020, 126: 105871.
- [13] 王聪,薛晓军,李恒,等.基于颜色校正和改进二维伽马函数的水下图像增强[J].电子测量与仪器学报,2021,35(2):171-178.
Wang C, Xue X J, Li H, et al. Underwater image enhancement based on color correction and improved 2D gamma function[J]. Journal of Electronic Measurement and Instrumentation, 2021, 35(2): 171-178.
- [14] Jordt A, Köser K, Koch R. Refractive 3D reconstruction on underwater images[J]. Methods in Oceanography, 2016, 15/16: 90-113.
- [15] Treibitz T, Schechner Y, Kunz C, et al. Flat refractive geometry[J]. IEEE Transactions on Pattern Analysis and Machine Intelligence, 2012, 34(1): 51-65.
- [16] 谢亮亮,屠大维,张旭,等.深海原位激光扫描双目立体视觉成像系统[J].仪器仪表学报,2020,41(6):106-114.
Xie L L, Tu D W, Zhang X, et al. Deep sea *in situ* binocular stereo vision imaging system with laser scanning[J]. Chinese Journal of Scientific Instrument, 2020, 41(6): 106-114.
- [17] Zhuang S F, Zhang X, Tu D W, et al. A standard expression of underwater binocular vision for stereo matching[J]. Measurement Science and Technology, 2020, 31(11): 115012.
- [18] Zhang C, Zhang X, Zhu Y K, et al. Model and calibration of underwater stereo vision based on the light field[J]. Measurement Science and Technology, 2018, 29(10): 105402.

Underwater Binocular Vision 3D Imaging with Active Speckle Projection

Zhuang Sufeng, Tu Dawei*, Liu Jianye

School of Mechatronic Engineering and Automation, Shanghai University, Shanghai 200072, China

Abstract

Objective In the vision-guided robot operation, it is necessary to acquire the 3D image of the target in the scene dynamically when there is relative motion between the target and the vision system. Binocular stereo vision can obtain images of the left and right cameras synchronously and quickly and has better dynamic adaptability compared with the 3D imaging methods characterized by scanning, such as laser radar and linear scanning structured light technology. The binocular stereo vision technology assisted by active speckle projection illumination enhances the texture information of the target surface and improves the matching accuracy of corresponding points of the left and right images. Thus, it is a simple and effective approach. At present, the research on the binocular stereo vision system with active speckle projection applied in the air is mature relatively, and many commercial products have been developed, such as the Kinect system of Microsoft, the Vic-3D measurement system of Correlation Solutions, and the Q-400 system of Dantec in Germany. However, when this technology is applied in the water, there are problems such as the pinhole model failure, unsatisfied matching conditions of polar constraints, and the image degradation caused by the underwater environment absorption and scattering of left and right images of the projected speckle. This will affect the matching accuracy of the corresponding points and the underwater 3D imaging effect.

Methods We rebuild an underwater binocular vision imaging model that actively projects speckle patterns based on the 4D parameter representation of light. The influence of the speckle pattern on the matching accuracy of underwater binocular corresponding points is analyzed based on MATLAB 2015b. The experimental device of underwater binocular vision dynamic 3D imaging system with active speckle projection is mainly composed of a speckle pattern projector and two cameras. The employed speckle pattern projector is a projector. The speckle pattern generated by the computer is projected on the underwater target by the projector, and the left and right cameras synchronously and quickly shoot the underwater moving object with the speckle pattern on the surface. According to the principle of binocular stereo vision, the 3D image of the underwater target is calculated.

Results and Discussions The simulation results of the relationship between speckle pattern and matching accuracy of underwater binocular imaging are shown in Fig. 6. With the rising speckle size, the maximum matching error first decreases and then increases. When the speckle size is between 3 pixel and 15 pixel, the maximum matching error is less than 0.7 pixel, and when the speckle size is 9 pixel, the matching accuracy is the highest. This is because when the speckle density is constant, too large or too small speckle is not conducive to matching, and the appropriate size of the speckle can enhance the matching clues of the corresponding points of the left and right images. Fig. 7 shows the influence of speckle density on the matching accuracy when the speckle size is 9 pixel. With the increase in speckle density, the maximum matching error first decreases and then increases. When the speckle density is 1.5% to 3.5%, the matching error is less than 0.6 pixel, and when the speckle density is 2%, the matching accuracy is the highest. Fig. 8 presents that the maximum matching error gradually increases with the decreasing object distance (from 2400 mm to 3600 mm), but the maximum matching error is still less than 1.1 pixel. This method has high matching accuracy. In addition, the purpose of the underwater experiment is to investigate the underwater dynamic 3D imaging error of the established experimental device. The experimental scenario is shown in Fig. 10. The projector is connected to the computer, the speckle density generated by the computer is 2%, and the speckle size is 9 pixel. The projector projects the speckle pattern diagonally downward on the underwater target surface. The underwater target is a standard ball that is suspended by a string at about 3 m in front of the experimental device. As shown in Fig. 11, the standard ball swings on the parallel plane of two cameras, the starting angle is about 50°, and the ball can swing freely when it is released at zero initial speed. It has different instantaneous linear speeds at different positions and has the maximum instantaneous speed at the lowest point. The maximum instantaneous speed is about 1.2 m/s. The 3D point cloud can be calculated based on the captured left and right images. Fig. 13 shows the 3D point cloud images at the corresponding positions in Fig. 12. The PolyWorks software is adopted to fit the obtained 3D point cloud into a sphere (picture-in-picture in Fig. 13). The diameter of the sphere and coordinates of the center of the sphere are obtained (data in the upper right corner of picture-in-picture), and the dynamic measurement error is obtained by comparing the diameter of the standard sphere. The dynamic imaging experiment has been operated on many times. The diameter error of the standard ball at the lowest point and the standard

deviation of the measured result are shown in Table 3. The experimental results show that the standard deviation of dynamic measurement error at the maximum instantaneous speed of the standard ball is 2.4 mm with a sound dynamic 3D imaging effect.

Conclusions We conduct a study on the underwater binocular stereo vision dynamic imaging technology based on the active speckle projection, analyze the influence of active speckle pattern projection on the matching accuracy of corresponding points of underwater binocular stereo vision, and establish the experimental device of underwater binocular vision dynamic 3D imaging system based on active speckle projection. The experimental results indicate that the underwater binocular stereo vision technology with the active speckle projection has a sound dynamic 3D imaging effect, and the dynamic measurement error is within the static error determined by the structure and system parameters of the binocular stereo vision experimental device.

Key words imaging systems; underwater binocular stereo vision; dynamic 3D imaging; underwater 3D reconstruction; active speckle projection